Nano Research 2015, 8(5): 1480–1496
DOI 10.1007/s12274-014-0632-7
Research Article
ISSN 1998-0124
CN 11-5974/O4

Shaped Pt–Ni nanocrystals with an ultrathin Pt-enriched shell derived from one-pot hydrothermal synthesis as active electrocatalysts for oxygen reduction

Jun Gu[1,§], Guangxu Lan[1,§], Yingying Jiang[2,§], Yanshuang Xu[1], Wei Zhu[1], Chuanhong Jin[2], and Yawen Zhang[1] (✉)

[1] *Beijing National Laboratory for Molecular Science, State Key Laboratory of Rare Earth Materials Chemistry and Applications, PKU-HKU Joint Laboratory in Rare Earth Materials and Bioinorganic Chemistry, College of Chemistry and Molecular Engineering, Peking University, Beijing 100871, China*

[2] *State Key Laboratory of Silicon Materials, Key Laboratory of Advanced Materials and Applications for Batteries of Zhejiang Province and School of Materials Science and Engineering, Zhejiang University, Hangzhou 310027, China*

[§] *These authors contributed equally to this work.*

Received: 3 September 2014
Revised: 21 October 2014
Accepted: 3 November 2014

KEYWORDS
Pt–NiPt–Ni alloy nanocrystals,
bimetallic catalysts,
oxygen reduction reaction,
dealloying,
aqueous-phase synthesis

ABSTRACT

Alloy nanocrystals (NCs) of Pt with 3d transition metals, especially Ni, are excellent catalysts for the oxygen reduction reaction (ORR). In this work, we, for the first time, demonstrated the water phase colloidal synthesis of Pt–*M* (*M* = Ni, Co and Fe) alloy NCs with tunable composition and morphology through a facile hydrothermal method. Pt–Ni alloy NCs synthesized with this method presented better ORR activity than commercial Pt/C catalysts. The X-ray energy dispersive spectra (EDS) mapping technique revealed that Pt-enriched shells existed on the as-synthesized Pt–Ni alloy NCs. About two atom thick layered Pt-enriched shells formed on $Pt_{50}Ni_{50}$ NCs and the thickness of the Pt-enriched shells increased as the Ni content increased. Furthermore, X-ray photoelectron spectroscopy analysis revealed that the oxidation level of the surface Pt atoms on the Pt–Ni alloy NCs decreased compared with monometallic Pt NCs, implying a decrease in the oxophilicity of the surface Pt atoms. Pt–Ni alloy NCs with lower oxophilicity of the surface Pt atoms give higher ORR activity. The most active alloy sample showed 13 times higher specific activity and six times higher mass activity at 0.9 V vs. a reversible hydrogen electrode when compared with commercial Pt/C. Pt–Ni alloy NCs also showed better durability than commercial Pt/C in long term ORR tests.

1 Introduction

Combustion of fossil fuel is the cause of many environmental problems. Proton exchange membrane fuel cells (PEMFC), possessing the advantages of high energy transfer efficiency, and clean, quiet and stable

Address correspondence to ywzhang@pku.edu.cn

performance, are a promising replacement for fossil fuel energy [1–4]. Pt particles supported on carbon black (Pt/C) is the state-of-the-art catalyst for oxygen reduction reaction (ORR), the cathodic reaction of PEMFC. However, monometallic Pt catalysts exhibit sluggish ORR activity at low overpotential. As revealed by the theoretical work of Norskov, Koper and others [5–7], ORR on a Pt surface is a four-step reaction and the fourth step—protonation, electronation and desorption of OH group on the Pt site—is the rate limiting step. Decreasing the oxophilicity, namely weakening the oxygen bonding to Pt atoms, can enhance the ORR activity of Pt-based catalysts. Numerous studies have shown that alloying Pt with iron group elements (Fe, Co and Ni, denoted as *M*), especially Ni, can increase the activity and simultaneously lower the usage of Pt, which offers a brighter future for PEMFC [8–13]. The lattice compression and the electron transfer from *M* to Pt [14–16] can lower the d-band center of the Pt atoms on the surface and thereby weaken the oxygen bonding.

Great efforts have been paid to the liquid-phase synthesis and the post-treatment of Pt–*M* alloy nanocrystals (NCs). The synthesis of Pt–*M* NCs was first realized in oleylamine (OM) [17–22]. Fang's group [23, 24] and Yang's group [25, 26] developed synthesis strategies for Pt–*M* nanocubes and nanooctahedrons in OM by introducing CO as reductant and facet-directing agent. Thermal treatment and acid treatment procedures could be used to remove the adsorbed OM molecules from Pt–*M* alloy NCs synthesized in OM, and produce a Pt-skeleton and a Pt-skin over Pt–*M* alloy NCs, which significantly enhanced the ORR specific activity of the nanocatalysts [27-30]. Recently, Stamenkovic et al. reported that Pt–Ni alloy frameworks can be prepared through the oxygen etching of solid Pt–Ni alloy NCs synthesized in OM and showed the highest ever ORR activity [31]. Pt–Ni alloy NCs dispersible in water could also be synthesized through solvothermal methods in benzyl alcohol as reported by Li's group [32–34] or in DMF as reported by Carpenter's group [35] and Strasser's group [36]. Water phase synthesis of Pt–*M* alloy NCs would be a potential environment-benign technique to prepare electrocatalysts ready for use. However, since the reduction potentials of M^{2+} cations are substantially lower than that of Pt^{2+} or Pt^{4+} in aqueous solution, it is still a challenge to simultaneously reduce Pt and *M* precursors and synthesize Pt–*M* alloy NCs in water.

Additionally, the composition and morphology evolution of the Pt–Ni alloy NCs during the ORR have attracted great attention recently [37–43]. Ni atoms near the surface of alloy NCs could be leached out during the voltage sweeps, which led to the formation of shells with Pt-skeleton structure [9, 39]. The thickness of the skeleton shell was dependent on the initial Pt:Ni ratio [39, 40]. Hollow structures could also form through the leaching of Ni from the alloy NCs, and the formation of the cavities on the alloy NCs during ORR was influenced by the alloy composition and particle size of the NCs [35, 41–43]. To avoid the loss of ORR activity resulting from serious leaching of 3d metals and increase the durability of the alloy catalysts, core–shell trimetallic NCs with Pt–*M* alloy shells were also explored extensively recently [44, 45].

In this work, poly(vinylpyrrolidone) (PVP) capped water-dispersible Pt–Ni, Pt–Co and Pt–Fe alloy NCs were synthesized with a facile hydrothermal method. To our knowledge, this is the first report of the water phase synthesis of alloy NCs of Pt and iron group metals. In this hydrothermal method, ammonium formate ($HCOONH_4$) was used as reductant, and ammonia and halide ions (Br^- or Cl^-) were introduced to coordinate with Pt^{2+} and narrow the gap between the reduction potentials of Pt^{2+} and M^{2+} precursors. The morphology and Pt:Ni ratio of the Pt–Ni alloy NCs could be tuned by changing the identity of the halide ions and the feeding ratio of Pt and Ni precursors. X-ray energy dispersive spectroscopy (EDS) mappings of the Pt–Ni alloy NCs obtained from hydrothermal synthesis showed that Pt atoms were enriched near the surface of the NCs. For $Pt_{50}Ni_{50}$ NCs, Pt-enriched shells with about two atomic layers were observed, and as the Ni content increased, the thickness of the Pt-enriched shells increased. X-ray photoelectron spectroscopy (XPS) analysis revealed that Pt atoms on the surface of Pt–Ni alloy NCs showed lower levels of oxidation compared with monometallic Pt NCs. Supported on carbon black, the Pt–Ni alloy NCs synthesized in this work showed enhanced ORR

activity compared with commercial Pt/C catalyst. The alloy sample with the highest ORR activity showed a 13 times enhancement in specific activity and six times enhancement in mass activity compared with commercial Pt/C at 0.9 V vs. reversible hydrogen electrode (RHE). Moreover, a strong correlation between the ORR specific activity and the surface Pt oxidation level was found, suggesting that a decrease in the oxophilicity of surface Pt promoted the ORR on Pt–Ni alloy NCs. The hydrothermally synthesized Pt–Ni alloy NCs also showed better durability than commercial Pt/C, and the alloy NCs with higher content of Pt were more stable during long term electrochemical tests.

2 Results and discussion

2.1 Hydrothermal synthesis and structure characterization of Pt–Ni alloy NCs

Figure 1(a) compares the reduction potential of different Pt^{2+} and Ni^{2+} species (left) and the reducing capacity of different reductants (right) and Fig. 1(b) shows the X-ray diffraction (XRD) patterns of metallic products obtained under different conditions. The simultaneous reduction of Pt^{2+} and Ni^{2+} precursors is very difficult because of the huge gap between the reduction potentials of the commonly used precursors of these two metals. The standard reduction potentials of the redox pairs of $[PtCl_4]^{2-}/Pt$ and Ni^{2+}/Ni in aqueous solution are 0.73 and −0.25 V, respectively, relative to the standard hydrogen electrode. This gap decreases by 0.16 V when considering the heat of mixing of Pt and Ni metals [46]. If a weak reductant such as formate ion was used, Ni^{2+} ions could not be reduced and only Pt particles were obtained (the black line in Fig. 1(b)). If a strong reductant such as BH_4^- ions was used, metal precursors would be reduced immediately at room temperature. Although part of the Ni^{2+} could be reduced in this situation, room temperature is not adequate for the formation of Pt–Ni alloys (the blue line in Fig. 1(b)). $HCOONH_4$ exhibited stronger reducing capacity than sodium formate under hydrothermal conditions, since the former decomposed into formic acid and ammonia at the reaction temperature (Fig. S1 in the Electronic Supplementary Material (ESM) shows the thermogravimetric analysis (TGA) curves of ammonium formate and sodium formate). Formic acid further decomposes into active CO or H species which possess strong reducing capacity. CO has also been considered as a significant species in the synthesis of Pt–Ni alloy NCs in previous reports [13, 23–26]. Pt–Ni formed when $HCOONH_4$ was used as a reductant, but the reducing efficiency of Ni^{2+} was very low (the red line in Fig. 1(b)). Furthermore, by introducing aqueous ammonia and a high concentration of halide ions (Br^- or Cl^-), Pt–Ni alloy NCs with higher Ni content were obtained (the green line in Fig. 1(b)). These reagents form stable coordination complexes

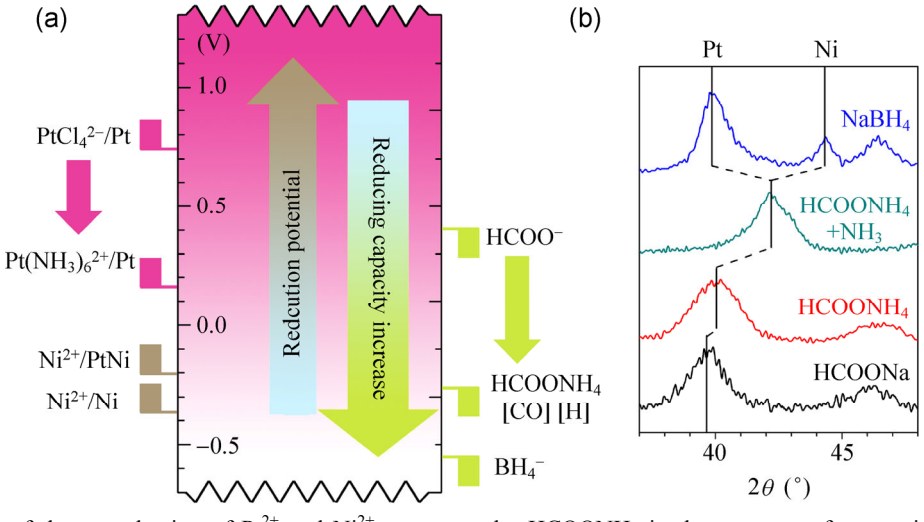

Figure 1 Principle of the co-reduction of Pt^{2+} and Ni^{2+} precursors by $HCOONH_4$ in the presence of ammonium and halide ions. (a) Comparison of the reduction potentials of different Pt^{2+} and Ni^{2+} precursors and the reduction capacities of different reductants. (b) (111) diffraction peaks of metallic NCs obtained by using different reductants and additives. The loading molar ratio of Pt:Ni was 1:2.

with Pt^{2+}, namely $Pt(NH_3)_6^{2+}$ (stability constant, lgK_s = 35), $PtCl_4^{2-}$ (lgK_s = 16) and $PtBr_4^{2-}$ (lgK_s = 21), which narrowed the reduction potential gap between Pt^{2+} and Ni^{2+}, and these strongly coordinated ligands may hinder the electron transfer from the reductant to Pt^{2+} and slow down the reduction of Pt^{2+} kinetically. Therefore, Pt–Ni alloy NCs were synthesized by reducing K_2PtCl_4 and $NiCl_2$ with $HCOONH_4$ in the presence of ammonia and potassium halide. Table 1 lists the identifications (IDs, in the format of "PtNi-*X*-*n*") of different Pt–Ni alloy NCs obtained from the hydrothermal method, in which "-*X*" (*X* = Br or Cl) represents the identity of the added halide ions and "-*n*" represents the Ni:Pt feeding ratio. It is noteworthy that no metallic product was obtained when only the Ni^{2+} precursor was loaded, indicating that the alloy process was indispensable for the reduction of Ni^{2+}.

Additionally, water, together with oxygen sealed in the container, at high temperature and high pressure may facilitate oxidative etching, and lead to the dissolution of part of the Ni^0 atoms on the surface. To verify this hypothesis, we treated Ni powder under the same hydrothermal conditions as those used to synthesize Pt–Ni alloy NCs (see Methods in the ESM). After the hydrothermal treatment, the concentration of Ni in the aqueous solution reached 12.2 μg·mL^{-1}. This oxidative etching process can also occur during the synthesis of Pt–Ni alloy NCs and lead to the formation of Pt-enriched shells over the alloy NCs, which was confirmed by EDS mapping and XPS analysis, as discussed later.

Table 1 Sample IDs and reagents used for synthesis of Pt–Ni alloy NCs

Sample ID	K_2PtCl_4 (mmol)	$NiCl_2$ (mmol)	Pt:Ni feeding ratio	Additive
PtNi-Br-1	0.03	0.03	1:1	KBr, 2.0 g
PtNi-Br-2	0.03	0.06	1:2	KBr, 2.0 g
PtNi-Br-3	0.02	0.06	1:3	KBr, 2.0 g
PtNi-Cl-1	0.06	0.06	1:1	KCl, 2.5 g
PtNi-Cl-2	0.06	0.12	1:2	KCl, 2.5 g
PtNi-Cl-3	0.04	0.12	1:3	KCl, 2.5 g

Figure 2(a) and 2(e) show the transmission electron microscopy (TEM) images of PtNi-Br-1 and PtNi-Cl-1,

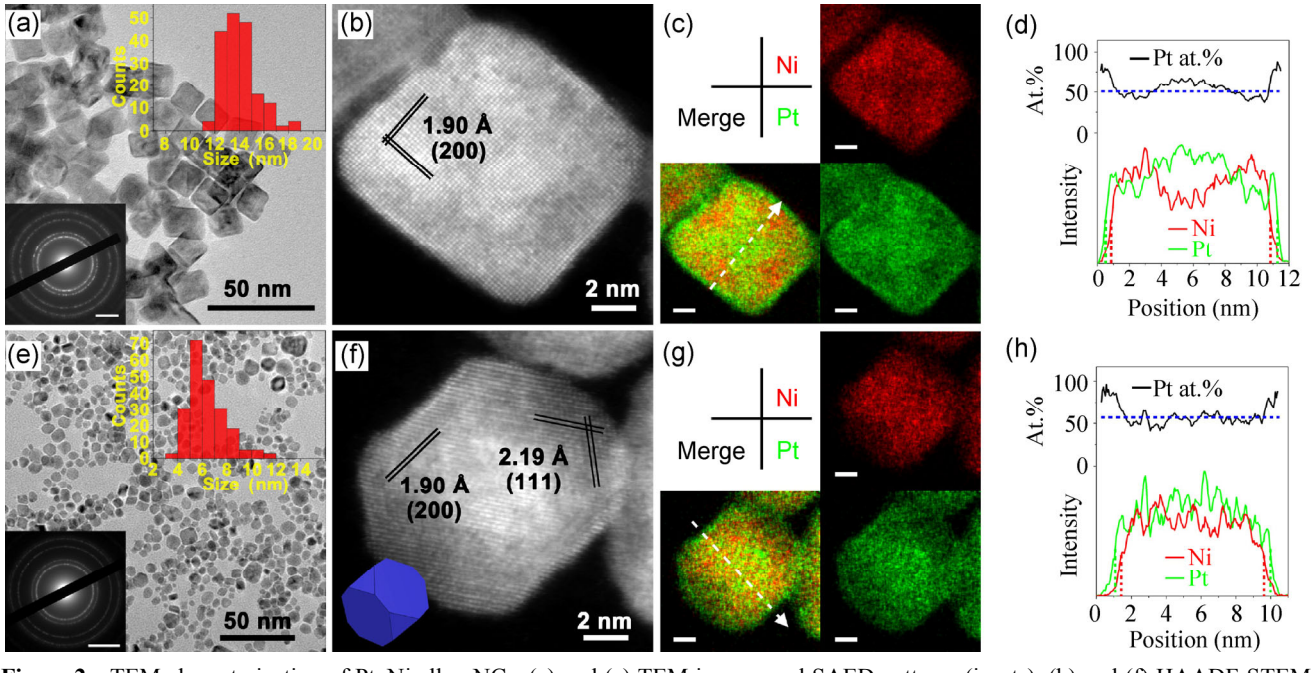

Figure 2 TEM characterization of Pt–Ni alloy NCs. (a) and (e) TEM images and SAED patterns (insets), (b) and (f) HAADF-STEM images, (c) and (g) EDS mappings and (d) and (h) the EDS line profiles of (a)–(d) PtNi-Br-1 and (e)–(h) PtNi-Cl-1. The size histograms are inserted in panels (a) and (e). Scale bars for the EDS mapping represent 2 nm. The EDS line profiles were collected along the white dashed arrow in the EDS mappings. The green and red curves correspond to Pt and Ni, respectively. The black curves show the atomic percentage of Pt and the blue dashed lines indicate the atomic percentage of Pt of the overall particle obtained from the EDS spectra. The green and red dashed vertical lines indicate the position of the half maximum of Pt and Ni line profiles respectively.

respectively. PtNi-Br-1 was mainly composed of nanocubes with a side length of 13.9 ± 1.2 nm. PtNi-Cl-1 was a mixture of truncated cubes, cubes and some NCs with irregular shapes and the average size was 8.4 ± 2.0 nm. The selectivity of truncated cubes in this sample was 70%. Figure 2(b) shows the high angle annular dark field scanning transmission electron microscopy (HAADF-STEM) image of a representative nanocube in PtNi-Br-1. According to the lattice fringes in this image, this nanocube was a single crystal enclosed by {100} facets, and a small amount of other facets were also exposed at the round edges and corners. Figure 2(f) shows a typical single-crystalline truncated cube in PtNi-Cl-1. Both {100} and {111} facets were mainly exposed on this NCs. Since halide ions blocked the {100} facets due to their strong adsorption on these facets, the crystal growth on the direction perpendicular to the {100} facets is suppressed, while growth in other directions is less influenced. Therefore, {100} facets of the crystal were maintained and nanocubes were obtained [47]. Previous work has shown that Br^- ions strongly direct Pt-based NCs to expose their {100} facets while Cl^- ions show lower facet-selectivity towards {100} facets compared with Br^- ions [48–50]. Figures 2(c) and 2(g) show the EDS-mappings of the NCs in Figs. 2(b) and 2(f), respectively, revealing that Pt and Ni formed an alloy in the NCs. Pt-enriched shells around the NCs can be seen in these EDS-mappings and line profiles in Figs. 2(d) and 2(h), implying the etching effect of water during the hydrothermal synthesis. The thicknesses of the Pt-enriched shells around the NCs (at half maximum as indicated by the green and red dashed vertical lines in the EDS line profiles) in PtNi-Br-1 and PtNi-Cl-1 are 4.4 ± 1.1 and 3.7 ± 0.6 Å, respectively, approximately equal to the thickness of two atomic layers.

Table 2 summarizes the Pt:Ni atomic ratio obtained from the methods of inductively coupled plasma atomic emission spectroscopy (ICP–AES), EDS, XPS and XRD, showing that Ni content in the alloy NCs could be increased by raising the loading ratio of Ni:Pt in the synthesis. The EDS spectra of the Pt–Ni alloy NCs are shown in Fig. S2 (in the ESM). The Pt content obtained from XPS was much higher than that obtained from other characterization methods for every sample, implying the existence of a Pt-enriched shell surrounding the alloy NCs. Figure 3 shows TEM images of PtNi-Br-2, PtNi-Br-3, PtNi-Cl-2 and PtNi-Cl-3. The size of Pt–Ni alloy NCs increases with decreasing Ni content. As shown by Figs. 3(a) and 3(b), PtNi-Br-2 and PtNi-Br-3 are mainly composed of concave nanocubes with the edge lengths of 20 ± 2 and 22 ± 2 nm, respectively. Figures 3(c) and 3(d) show the EDS mapping and line profile of a representative NC in PtNi-Br-3. Similar to PtNi-Br-1, Pt:Ni ratio in this sample was higher near the surface than inside the NC, as shown by the black curve in Fig. 3(d). The Pt-enriched shells (at half maximum) on this sample were 1.4 ± 0.6 nm in thickness, thicker than that on PtNi-Br-1, implying a higher level of water etching during the hydrothermal synthesis. The variation of the thickness of the shells was also larger. Pt content was highest at the corners of the concave nanocubes. During the formation of Pt–Ni alloy NCs, galvanic replacement between $PtCl_4^{2-}$ and Ni atoms on the NCs surface occurred. Since the {100} facets of the NCs were blocked by adsorbed Br^- ions, the Pt atoms were deposited on the eight corners of the nanocubes. Therefore, the specific adsorption of Br^- ions on {100} facets guided the deposition direction of Pt and leading

Table 2 Atomic ratio of Pt:Ni in different samples obtained from ICP–AES, EDS, XPS and XRD analyses

Sample ID	Before HAc treatment				After HAc treatment		
	ICP–AES	EDS	XPS	XRD	ICP–AES	EDS	XPS
PtNi-Br-1	52:48	50:50	67:33	61:39	52:48	51:49	75:25
PtNi-Br-2	34:66	38:62	56:44	49:51	38:62	41:59	64:36
PtNi-Br-3	24:76	33:67	54:46	38:62	25:75	33:67	67:33
PtNi-Cl-1	46:54	53:47	72:28	54:36	52:48	58:42	80:20
PtNi-Cl-2	31:69	35:65	62:38	38:62	35:65	37:63	73:27
PtNi-Cl-3	21:79	30:70	56:44	29:71	24:76	32:68	71:29

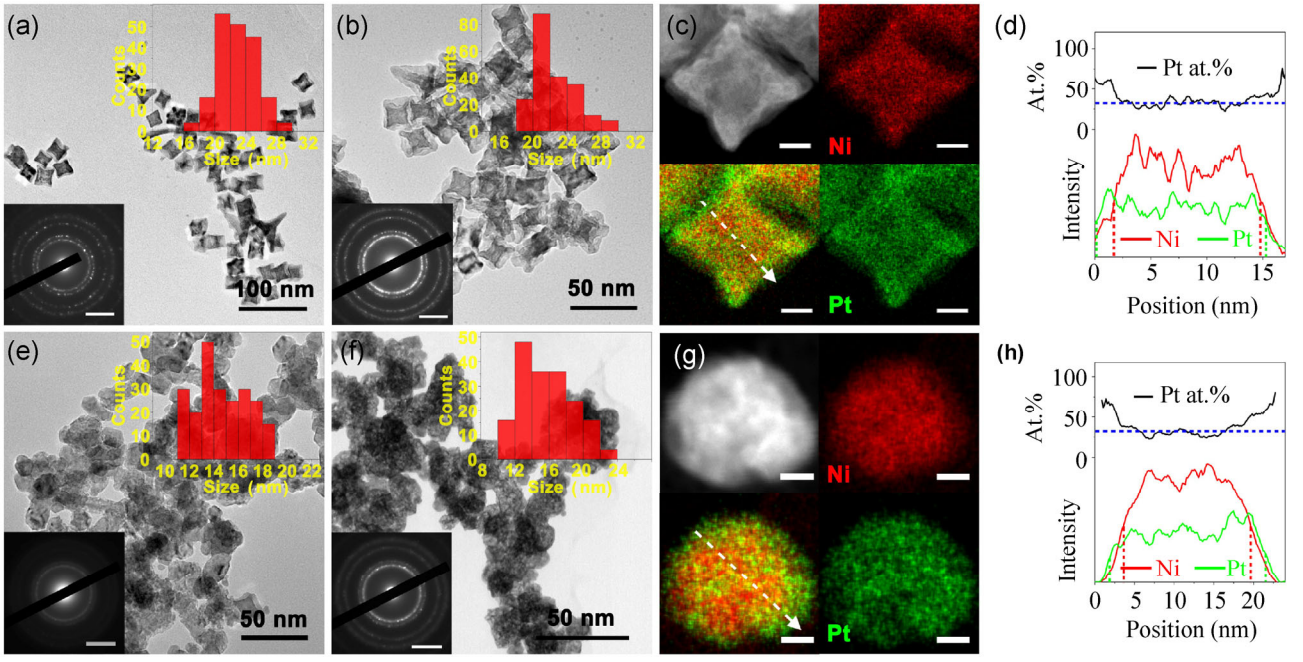

Figure 3 TEM characterization of Pt–Ni alloy NCs. TEM images and SAED patterns of (a) PtNi-Br-2, (b) PtNi-Br-3, (e) PtNi-Cl-2 and (f) PtNi-Cl-3. (c) and (g) EDS mappings and (d) and (h) the EDS line profiles of (c) and (d) PtNi-Br-3 and (g) and (h) PtNi-Cl-3. The size histograms were inserted in the corresponding TEM images. The scale bars in (c) and (g) represent 5 nm. The EDS line profiles were collected along the white dashed arrow in the EDS mappings. The green and red curves correspond to Pt and Ni, respectively. The black curves show the atomic percentage of Pt and the blue dashed lines indicate the atomic percentage of Pt of the overall particle obtained from the EDS spectra. The green and red dashed vertical lines indicate the position of the half maximum of Pt and Ni line profiles respectively.

to the concave morphology and Pt-enriched corners. Similar phenomena were also observed in previous work on Pt–Cu [51] and Pt–Pd [52] bimetallic concave nanocubes. PtNi-Cl-2 is composed of the aggregates of nano-polyhedrons with the average size of 15 ± 2 nm (Fig. 3(e)). The alloy NCs of PtNi-Cl-3 were porous, as shown in Fig. 3(f), suggesting that the etching effect of water on the alloy NCs became substantially higher as the Ni content increased. Figures 3(g) and 3(h) show the EDS mapping and line profile of a representative alloy NC in PtNi-Cl-3. Pt-enriched shells with an average thickness (at half maximum) of 1.6 ± 0.7 nm were observed on the alloy NCs, thicker than that on PtNi-Cl-1.

Solid curves in Fig. 4 show the XRD patterns of the Pt–Ni NCs obtained from hydrothermal synthesis. The diffraction peaks were located between the standard diffraction peaks of fcc Pt and fcc Ni with the corresponding index, indicating that Pt and Ni formed an alloy in the NCs. No diffraction peaks were detected before (111) peaks, implying that Pt and Ni were distributed randomly in the alloy instead of forming ordered intermetallics. The diffraction peaks shifted to higher angle as the Ni content increased, since the atomic radius of Ni is smaller than that of Pt. It is noteworthy that two alloy phases with different compositions could be detected in the Ni-rich samples, as shown by red and black arrows in Fig. 4. This phenomenon was also observed in Pt_xNi alloy NCs (x< 3) synthesized in DMF [35]. The etching of Ni-rich phases in these samples is a possible reason for the formation of the Pt-rich phases. Rietveld refinement analysis was used to calculate the composition and proportion of each alloy phase, as listed in Table S1 (in the ESM). Since the Pt:Ni ratio varied around a certain value within and among particles, which broadens the diffraction peaks, the domain size deduced from the peak width in the XRD patterns were smaller than the average particle size obtained in TEM images. Since the ideal Vegard's law underestimates the lattice constant according to a study on bulk Pt–Ni alloy [53], the Pt:Ni ratios calculated according

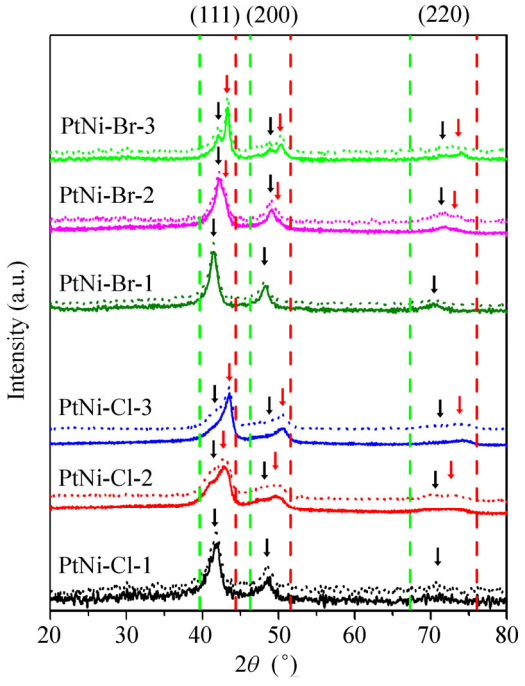

Figure 4 XRD patterns of different Pt–Ni alloy NCs. Solid lines correspond to the samples before the HAc treatment and dashed lines correspond to the HAc-treated samples. Positions of standard diffraction peaks of pure Pt (no. 01-1190) and Ni (no. 01-1258) are marked by the vertical dashed lines in green and red, respectively.

to Vegard's law were higher than those obtained from ICP–AES and EDS, as shown in Table 2.

To dissolve the Ni atoms on the surface and transform the Pt–Ni alloy NCs into a structure which is stable in acidic electrolytes, HAc treatment of these hydrothermal synthesized NCs was used. Table 2 compares the Pt:Ni ratios and Fig. 4 shows the XRD patterns of Pt–Ni alloy NCs before and after HAc treatment. The Ni content obtained from ICP–AES decreased slightly (<6%) while that obtained from XPS dropped more (8%–15%). Moreover, the XRD patterns were almost unchanged after the HAc treatment. These results indicate that only the Ni atoms in the outermost few atomic layers were dissolved while Ni atoms inside the alloy NCs were protected against the acid. The Pt-enriched shell over the alloy NCs transformed into a Pt-skeleton structure after this HAc treatment. Figure S3 (in the ESM) shows the EDS mappings of the Pt–Ni alloy NCs after the acid treatment. The green edges in the EDS mappings showed the Pt-shell of the Pt–Ni alloy NCs. Additionally, as the bulk Ni content increased, more Ni atoms near the surface were dissolved during the HAc treatment, as indicated by the XPS data in Table 2, implying thicker Pt-skeleton shells were formed.

XPS spectra were used to investigate the surface states of the Pt–Ni alloy NCs. Figure S4 (in the ESM) shows the representative survey XPS spectra of the hydrothermally synthesized Pt–Ni alloy NCs. Figure 5(a) compares spectra in the Ni $3p_{3/2}$-region of Pt–Ni alloy NCs before and after the HAc treatment, respectively, which can be fitted to three peaks corresponding to Ni^0 (852.4–852.6 eV), Ni^{2+} (855.1–855.5 eV) and the satellite feature (858.0–860.6 eV) [54, 55]. Due to the high oxophilicity of Ni, Ni atoms on the surface of Pt–Ni alloy NCs before the HAc treatment are oxidized and give rise to the Ni^{2+} state detected by the XPS analysis. The intensity of the Ni^{2+} peak decreased dramatically for the sample after the HAc treatment,

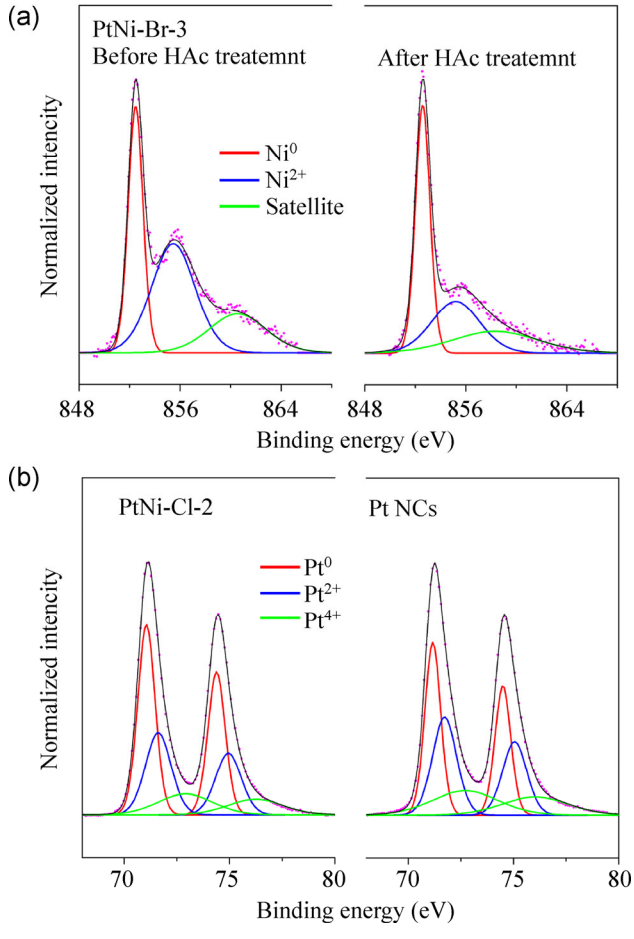

Figure 5 High resolution XPS spectra in the (a) Ni $2p_{3/2}$ region of PtNi-Br-3 (left) before and (right) after the HAc treatment and in the (b) Pt 4f region of (left) PtNi-Cl-2 and (right) hydrothermally synthesized Pt NCs after HAc treatment. The backgrounds were subtracted from the spectra.

indicating that the surface Ni atoms on the alloy NCs were dissolved during the HAc treatment. The XPS spectra in Pt 4f region were fitted to three doublets assigned to Pt^0 ($4f_{7/2}$, 71.1–71.3 eV), Pt^{2+} ($4f_{7/2}$, 71.7–71.9 eV) and Pt^{4+} ($4f_{7/2}$, 73.3–74.1 eV) [56, 57]. The percentage of Pt in each oxidation state of Pt–Ni alloy NCs did not change significantly after HAc treatment. Figure 5(b) and Table S2 (in the ESM) compares the XPS spectra in the Pt 4(f) region of Pt–Ni alloy NCs and hydrothermally synthesized Pt NCs after the HAc treatment. Pt element with positive valence states corresponds to surface Pt atoms oxidized by adsorbed O-species. Thus, a higher proportion of Pt in positive valence states indicates stronger oxophilicity of the Pt surface. HAc treated Pt–Ni alloy NCs show lower proportion of Pt^{n+} (n = 2, 4) state than monometallic Pt NCs, indicating that the oxophilicity of the Pt shell on these Pt–Ni alloy NCs was suppressed. Some previous theoretical and experimental studies have demonstrated that alloying Pt with 3d metals causes Pt–Pt compression on the surface, leading to the broadening and sinking of the d-band of the surface Pt atoms. Our XPS result showed a decreased oxophilicity of the Pt atoms on the surface of the Pt–Ni alloy NCs, which is in accordance with the d-band theory that the oxygen adsorption weakens as the d-band center decreases in energy.

2.2 Hydrothermal synthesis and characterization of Pt–Co and Pt–Fe alloy NCs

By changing the $NiCl_2$ to $CoCl_2$ or $FeSO_4$, the hydrothermal method in this work could be further used to synthesize Pt–Co and Pt–Fe alloy NCs. The sample IDs, reagents used for the synthesis and the element analysis results are listed in Table S3 (in the ESM). The reduction potentials of Co^{2+}/Co and Fe^{2+}/Fe are −0.28 and −0.44 V, respectively, lower than that of Ni^{2+}/Ni. Consequently, the reducing efficiency decreased in the order Ni > Co > Fe when the loading ratios of Pt:M (M = Ni, Co and Fe) were same. Figure 6(a) shows the XRD patterns of PtCo-Cl-1 and PtFe-Cl-1. The diffraction peaks of ordered intermetallics were not detected. A series of weak peaks of Fe_3O_4 (JCPDS no. 01-1111) could be detected in the diffraction pattern of PtFe-Cl-1, as indicated by red triangles. Figures 6(b) and 6(c) show the TEM images of PtCo-Cl-1 and PtFt-Cl-1, respectively, and Fig. S5 (in the ESM) shows the corresponding high resolution TEM (HRTEM) images. PtCo-Cl-1 consisted of polyhedrons with the size of 7.0 ± 1.8 nm, and PtFe-Cl-1 was composed of crystallites with the size of 3.0 ± 0.4 nm coalesced into dendritic structures. Figure S6 (in the ESM) shows the EDS spectra of Pt–Co and Pt–Fe alloy NCs. Because of the existence of Fe_3O_4 particles in PtFe-Cl-1, the Pt:Fe ratio of this sample obtained from ICP–AES and EDS was substantially higher than that calculated from XRD data listed in Table S3 (in the ESM).

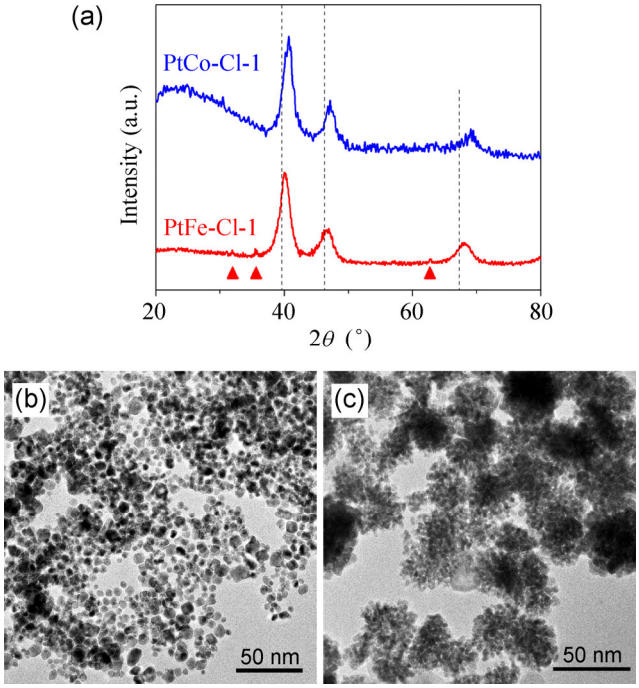

Figure 6 Characterization of Pt–Co alloy NCs and Pt–Fe alloy NCs synthesized with the hydrothermal method. (a) XRD patterns of PtCo-Cl-1 (up) and PtFe-Cl-1 (down). Red triangles indicate the weak diffraction peaks of Fe_3O_4. The black vertical dashed lines show the position of diffraction peaks of pure Pt. TEM images of (b) PtCo-Cl-1 and (c) PtFe-Cl-1.

When the loading amount of M (M = Co or Fe) increased, the content of M in the alloy NCs increased, as indicated by the XRD pattern in Fig. S7 (in the ESM). However, a large amount of Co_3O_4 or Fe_3O_4 particles formed simultaneously and could not be dissolved by the HAc treatment. Diffraction peaks of these oxides are labeled in Fig. S7 (in the ESM). As shown by the TEM images of PtCo-Cl-3 and PtFe-Cl-3 in Fig. S8 (in the ESM), these samples were composed of aggregates of small alloy NCs surrounded by large oxide particles with lower contrast.

2.3 Electrochemical study of hydrothermally synthesized Pt–Ni alloy NCs

After HAc treatment and washing five times with deionized water, the NCs were supported on carbon black (Vulcan XC-72R) by ultrasound treatment (Fig. S10, in the ESM). Trace amount of halide ions (<0.3 at.%) remained on the NCs after the washing procedures, which was indicated by some weak peaks in the EDS spectra (Fig. S2). After the catalysts were loaded on the glassy carbon electrode, UV–ozone treatment [58, 59] was carried out to break down the long-chain stabilizer PVP on the surface of carbon supported Pt–Ni alloy NCs, and part of the fragments could be removed by rinsing the electrode with water. IR spectra (Fig. S9, in the ESM) show that about half of the PVP was removed from the alloy NCs after the washing step and UV–ozone treatment. The upper part of Fig. 7 shows the cyclic voltammetry (CV) curves of the hydrothermally synthesized Pt–Ni alloy NCs and commercial Pt/C. In this figure, the light blue stripe represents the charging current of the double layer, and two pairs of adsorption–desorption processes occurred on Pt surface, namely the under-potential deposition (UPD) of H, stripping of UPD-H, adsorption and desorption of O-species, can be observed, indicating that the surface of HAc treated Pt–Ni alloy NCs was occupied by Pt atoms. The onset potentials of O-species desorption on Pt–Ni alloy NCs show anodic shift in contrast with that on commercial Pt/C, as indicated by the arrow, suggesting that the adsorption of oxygen on the surface of Pt–Ni alloy NCs became substantially weaker.

The electrochemical active surface area (ECSA) of the catalysts was calculated from H_{upd} adsorption/desorption regions and CO stripping curves (the lower part of Fig. 7) and listed in Table 3 and Table S4 (in the ESM). In our experimental results, ECSAs obtained from both methods were quite close for monometallic Pt/C and Pt–Ni alloy NCs (the differences were less than 5%). It is noteworthy that the adsorption of UPD-H on the Pt skin on Pt_3Ni (111) surface was suppressed since the electronic structure of surface Pt was modified by the Ni-rich sublayer, and consequently the ECSA is substantially underestimated when using the charge of H_{upd} [29, 31, 60, 61]. However, for the skeleton type Pt shell over Pt–Ni alloy NCs formed from the leaching of Ni-rich alloy NCs, CO stripping and H_{upd} gave similar ECSA [29, 31, 40, 60]. The ECSA values of the hydrothermally synthesized Pt–Ni alloy NCs obtained from both methods were close, implying these Pt–Ni alloy NCs adopted a skeleton type Pt surface. The ECSA decreased as the Ni content increased because of the increase in particle size, except that PtNi-Cl-3/C represented the highest ECSA, due to the

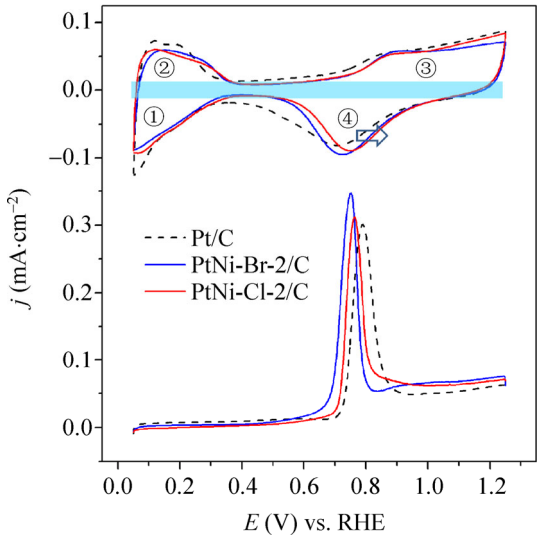

Figure 7 CV curves (top) and CO stripping curves (bottom) of carbon supported PtNi-Br-2/C (blue lines), PtNi-Cl-2/C (red lines) and the commercial Pt/C (black dashed lines) with a scan speed of 50 $mV \cdot s^{-1}$ in N_2 saturated 0.1 M $HClO_4$. Before the collection of CO stripping curve, the working electrode was kept at 0.1 V vs. RHE and the electrolyte was bubbled with CO for 5 min followed by N_2 for 10 min.

Table 3 ECSA and ORR activity at 0.9 V vs. RHE of carbon black supported alloy NCs and monometallic Pt/C

Sample ID	ECSA ($m^2 \cdot g_{Pt}^{-1}$)	Mass activity ($A \cdot mg_{Pt}^{-1}$)	Specific activity ($mA \cdot cm^{-2}$)
PtNi-Br-1/C	40 ± 3	0.60 ± 0.08	1.48 ± 0.11
PtNi-Br-2/C	37 ± 3	0.83 ± 0.05	2.25 ± 0.10
PtNi-Br-3/C	33 ± 4	0.58 ± 0.04	1.76 ± 0.14
PtNi-Cl-1/C	47 ± 2	0.83 ± 0.03	1.76 ± 0.13
PtNi-Cl-2/C	37 ± 5	1.01 ± 0.14	2.69 ± 0.12
PtNi-Cl-3/C	51 ± 4	0.84 ± 0.05	1.67 ± 0.04
PtCo-Cl-1/C	50 ± 6	0.51 ± 0.08	1.02 ± 0.11
PtFe-Cl-1/C	65 ± 4	0.34 ± 0.04	0.53 ± 0.07
Commercial Pt/C	84 ± 5	0.17 ± 0.01	0.20 ± 0.02
Hydrothermal Pt/C	42 ± 7	0.09 ± 0.02	0.21 ± 0.04

porous structure of this sample.

Figure 8(a) shows the ORR polarization curves of carbon black supported Pt–Ni alloy NCs, Pt NCs (Fig. S10(g), in the ESM) and commercial Pt/C catalyst, and Fig. S11 (in the ESM) shows those of the other samples. The iR-drop was compensated for each sample and the high frequency resistance of the setup is listed in Table S4 (in the ESM). The half wave potential of PtNi-Br-2/C and PtNi-Cl-2/C are respectively 48 and 60 mV higher than that of commercial Pt/C. Figure 8(b) and Table 3 compare the ORR mass activity normalized to the mass of Pt and specific activity normalized to ECSA at 0.9 V vs. RHE. PtNi-Cl-2/C showed highest mass activity and specific activity, namely 1.01 A·mg_{Pt}^{-1} and 2.69 mA·cm^{-2}, about six times and 13 times of that of commercial Pt/C, respectively.

Moreover, as shown in Fig. 8(c), the ORR specific activity of hydrothermally synthesized Pt and Pt–Ni alloy catalysts showed a positive correlation with the ratio of $Pt^0/(Pt^0+Pt^{n+})$ obtained from XPS data fitting in Fig. 5 and Table S2 (in the ESM). As discussed in Section 2.1, a higher proportion of Pt^{n+} state implies a higher oxophilicity of the surface Pt atoms, and a higher fraction of Pt^0 state indicates a suppressed oxophilicity. Although the XPS data were collected in an ultra-high vacuum environment which is far from the real electrochemical conditions, considering that every sample was prepared with a similar hydrothermal method, followed by the same post-treatment procedure, and every XPS spectrum was collected under the same conditions, these *ex situ* data still reflect the intrinsic oxophilicity of different samples. The alloy samples showed suppressed oxophilicity, which weakened the OH adsorption and is beneficial to the rate limiting step of ORR, i.e. protonation, electronation

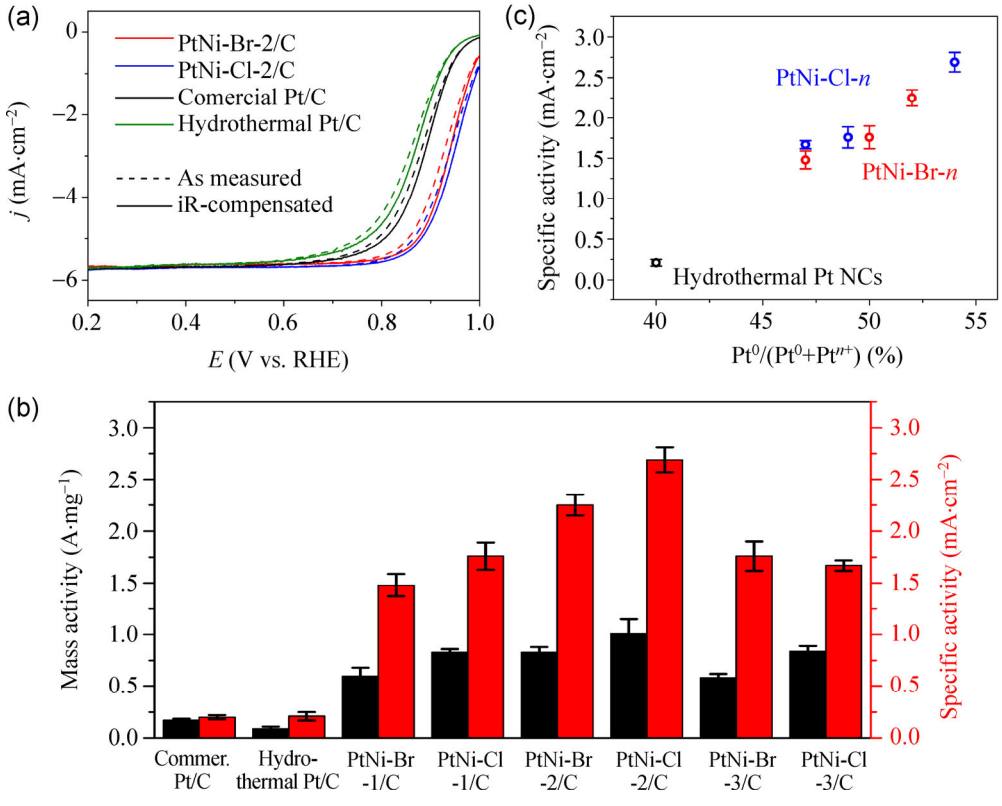

Figure 8 ORR activity of carbon supported Pt–Ni alloy NCs and monometallic Pt/C catalysts. (a) ORR polarization curves of carbon black supported Pt–Ni alloy NCs, commercial Pt/C and hydrothermally synthesized Pt/C. The loading amount of Pt was 5.0 μg for each sample. These curves were collected on a rotating disk electrode (RDE) with a rotation speed of 1,600 rpm in the anodic scan with a scan speed of 20 mV·s^{-1} in O_2 saturated 0.1 M $HClO_4$. The dashed lines show the as measured curves without iR-drop correction and the solid lines show the curves with iR-compensation. The capacitance current was subtracted. The current density is normalized to the geometric area of RDE. (b) Comparison of mass activity and specific activity at 0.9 V vs. RHE of each sample. (c) Plot of specific activity depending on the atomic ratio of $Pt^0/(Pt^0+Pt^{n+})$ obtained from XPS analysis as a scale of the oxophilicity of surface Pt atoms.

and desorption of OH groups from Pt sites, and led to the enhancement in ORR activity [5–7]. Figure 8(b) also shows the dependence of the ORR specific activity on the composition of the Pt–Ni alloy catalysts. The highest ORR specific activity was achieved at a medium Ni:Pt ratio, which has also been observed on Pt–Ni alloy NCs synthesized with other methods [35, 39]. On the one hand, the lattice distance decreased as the Ni content increased, which led to the Pt–Pt compression on the surface and weakened the bonding of OH species [14, 15]. On the other hand, the Pt-enriched shells (defined as the average distance between the half-maximum positions of Pt and Ni elements in the EDS line profile) on Pt–Ni alloy NCs became thicker as the Ni content increased, as revealed by Figs. 2 and 3. The Pt-enriched shells transformed into a skeleton structure during the HAc treatment. Thick Pt-enriched shells and skeleton overlayers on the Pt–Ni alloy NCs are detrimental to ORR since the lattice compression was released [39, 40]. The particle size also influenced the catalytic performance of Pt–Ni alloy NCs. Previous studies have shown that the ORR specific activity of Pt and Pt alloy NCs increased as the particle size increased, since the fraction of the undercoordinated atoms on the edges and corners—which showed strong oxophilicity and blocked the access of oxygen molecules—was lower on larger particles [8, 21]. However, this rising trend in ORR specific activity was negligible when the particle size increased beyond 10 nm, just like the case of the hydrothermally synthesized Pt–Ni alloy NCs in this work. Therefore, the particle size mainly affects the specific surface area and the ORR mass activity of the catalysts.

The electrocatalytic properties of carbon black supported hydrothermally synthesized Pt–Co and Pt–Fe alloy NCs were also investigated. These samples represent higher specific surface area but lower ORR specific activity than Pt–Ni alloy catalysts, as shown in Table 3 and Fig. S12 (in the ESM). Since the reducing efficiency of Co and Fe precursors under hydrothermal conditions is lower than that of Ni, as discussed in Section 2.2, the content of Co and Fe in the alloy catalysts could only reach 26% and 13%, respectively, which is probably lower than the optimum Co or Fe content to achieve the highest ORR activity.

To test the stability of hydrothermally synthesized Pt–Ni alloy NCs in long term ORR, 10,000 cycles of voltage sweeps in the range of 0.6–1.0 V were applied [31, 62–65]. Figure 9 shows the TEM images and the Ni content obtained from EDS analysis of Pt–Ni alloy NCs after the voltage sweeps. The Ni content decreased after the potential sweeps, indicating that the Pt skeleton shell over the Pt–Ni alloy NCs reconstructed during the potential sweeps, leading to the exposure and leaching of the Ni atoms in the alloy. The loss of Ni content was lower for Pt-rich sample, indicating that Pt-rich Pt–Ni alloy NCs were more stable towards electrochemical leaching. The Pt-rich sample (PtNi-Cl-1) also showed better morphology stability, and retained the solid structure after the voltage sweeps (Fig. 9(a)), while PtNi-Cl-2/C evolved from a solid to a porous structure like PtNi-Cl-3, due to the leaching of the NCs (Fig. 9(b)). Figure 10 compares the ECSA and ORR polarization curves of Pt–Ni alloy NCs and commercial Pt/C before and after the voltage sweeps. Pt–Ni alloy NCs with lower Ni content retained higher ECSA and ORR activity. The ECSA

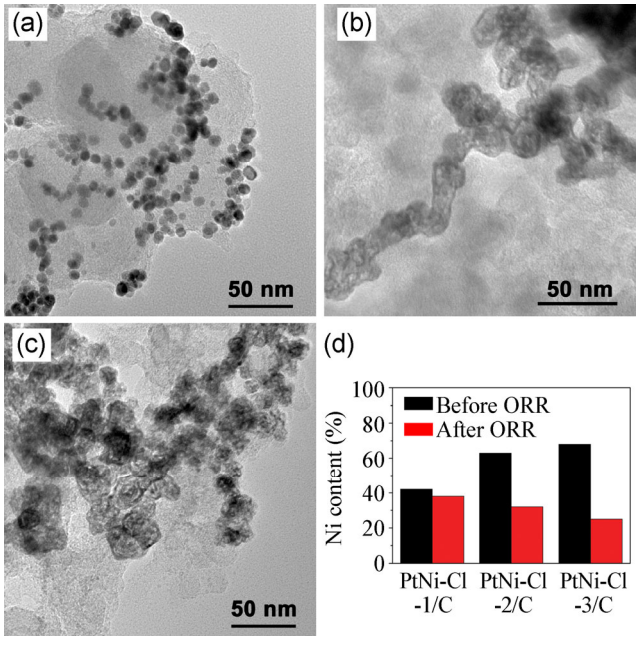

Figure 9 TEM characterization of the carbon supported Pt–Ni alloy NCs after ORR tests. TEM images of carbon black supported (a) PtNi-Cl-1/C, (b) PtNi-Cl-2/C and (c) PtNi-Cl-3/C after 10,000 cycles of voltage sweeps in the range of 0.6–1.0 V vs. RHE with a scan speed of 200 $mV \cdot s^{-1}$ in O_2 saturated 0.1 M $HClO_4$. (d) Comparison of Ni molar content of Pt–Ni alloy NCs (obtained from EDS) before (black) and after (red) the voltage sweeps.

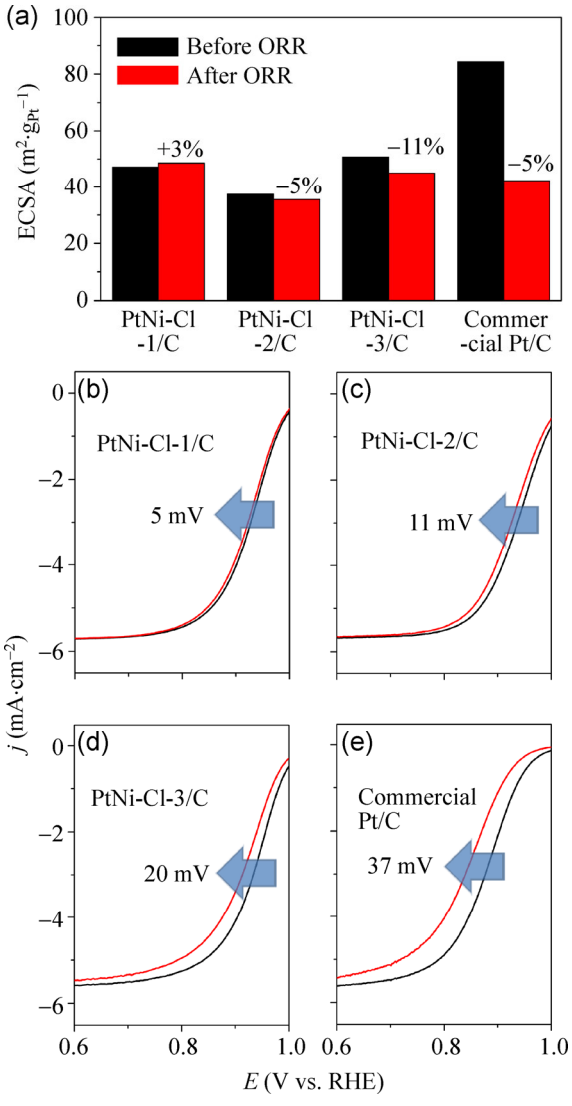

Figure 10 Comparison of the electrochemical properties of carbon black supported Pt–Ni alloy NCs and Pt/C catalysts before and after the long term ORR tests. (a) ECSAs of Pt–Ni alloy NCs and commercial Pt/C before (black) and after (red) the 10,000 cycles of voltage sweeps. (b)–(e) ORR polarization curves of carbon black supported Pt–Ni alloy NCs and commercial Pt/C before (black) and after (red) the 10,000 cycles of voltage sweeps. The cathodic shift of half wave potential for each sample was marked on each panel.

loss and the further dealloying of the Ni-rich NCs led to a decrease in the ORR activity. The cathodic shift of the ORR half wave potential of each sample is shown in Figs. 10(b)–10(e) and Fig. S13 (in the ESM), and indicates that hydrothermally synthesized Pt–Ni alloy NCs exhibited better durability than commercial Pt/C during long term ORR tests.

3 Conclusions

We have developed a facile hydrothermal method to prepare Pt–*M* (*M* = Ni, Co and Fe) alloy NCs, in which $HCOONH_4$ served as the reductant, and ammonia and halide ions were used to narrow the gap between the reduction potentials of Pt^{2+} and M^{2+} ions and slow down the reduction rate of Pt^{2+}. The composition and the morphology of the Pt–Ni alloy NCs could be tuned by changing the Pt:Ni feeding ratio and the halide ions used in the synthesis. Since water, together with oxygen, exhibited etching ability towards metallic Ni under the hydrothermal conditions, Pt-enriched shells formed as the Pt–Ni alloy NCs were obtained, as revealed by EDS mapping and XPS analyses. About two atomic layer thick Pt-enriched shells formed on $Pt_{50}Ni_{50}$ NCs and the thickness of the Pt-enriched shells increased as the Ni content increased. Moreover, XPS spectra revealed that surface Pt atoms on the Pt–Ni alloy NCs showed much lower oxidation level than that on monometallic Pt NCs, implying the oxophilicity of the surface Pt atoms was suppressed. The decrease in the oxophilicity of the surface Pt atoms led to the enhancement in the ORR activity of the Pt–Ni alloy NCs. The Pt–Ni alloy NCs also exhibited better durability during long term ORR tests than Pt/C, and the sample with higher Pt content showed better durability.

The specific activity of the hydrothermally synthesized Pt–Ni alloy NCs showed a 13 times enhancement compared with commercial Pt/C, which was in line with reports on Pt–Ni alloy catalysts synthesized by other methods [24, 35, 36]. However, due to the slow nucleation rate and fast growth rate, the hydrothermal method provided Pt–Ni alloy NCs with sizes near or larger than 10 nm, which have lower specific surface areas than commercial Pt/C and only a six-fold mass activity enhancement compared with commercial Pt/C was achieved; this is lower than those of the most active Pt alloy catalysts ever reported (3.3 $A \cdot mg_{Pt}^{-1}$ @ 0.9 V [61] and 1.6 $A \cdot mg_{Pt}^{-1}$ @ 0.95 V [31]). Enlightened by the seeded growth method [44, 45, 63, 66, 67], a promising strategy to prepare smaller Pt–Ni alloy NCs based on hydrothermal methods is to introduce tiny metal seeds to replace the nuclei formed slowly *in situ*. By increasing the seed population, the size of the nanoparticles can be reduced, thus increasing the

specific surface area and maxmizing the mass activity. Constructing Pt–Ni nanoframworks by the etching of Ni-rich alloy NCs is another useful strategy to increase the specific surface area of the samples, giving high mass activities [31]. Furthermore, this work provides a robust way to control the reduction efficiency of dual metal precursors and a facile strategy to prepare complex bimetallic NCs combining noble and non-noble metal in an aqueous phase. The resulting materials can be directly used as electrocatalysts and other aqueous-phase catalysts with excellent performances.

4 Methods

4.1 Chemicals

K_2PtCl_4 (A.R., Shenyang Institute of Nonferrous Metals), $NiCl_2{\cdot}6H_2O$ (A.R., Beijing Yili Fine Chemical Reagent Corp.), ammonium formate ($HCOONH_4$; A.R., Beijing Yili Fine Chemical Reagent Corp.), PVP (*M*w = 29,000, Sigma-Aldrich), KBr (A.R., Xilong Chemical Industry Co. Ltd.), KCl (A.R., Beijing Chemical Works), ammonium hydroxide ($NH_3{\cdot}H_2O$; A.R., Beijing Chemical Works), acetic acid (HAc; A.R. Beijing Tongguang Chemical Industry Co. Ltd.), carbon black (Vulcan XC-72R, Cabot), Pt/C catalyst (20 wt.% Pt, Shanghai Hesen Electric Co. Ltd.), perchloric acid ($HClO_4$; A.R., Beijing Chemical Reagent Corp.), methanol (MeOH; HPLC, Xilong Chemical Industry Co. Ltd.), and Nafion (Alfa Aesar) were used as received. Ultrapure N_2 and O_2 were used in the electrochemical tests. The water used in all experiments was ultrapure (Millipore, 18.2 MΩ).

4.2 Hydrothermal synthesis of Pt–Ni alloy NCs

The hydrothermal synthesis was carried out in 25 mL Teflon-lined containers sealed in stainless steel autoclaves. In the synthesis of PtNi-Br-1, 100 mg of PVP, 63 mg of $HCOONH_4$ and 2.0 g of KBr were first loaded into the container and dissolved in 8 mL of deionized water. Then, 0.03 mmol of $NiCl_2$, 38 μL of $NH_3{\cdot}H_2O$ (25%–28%) and 0.03 mmol of K_2PtCl_4 were added and dissolved in sequence. Finally, the solution was diluted to 15 mL by adding deionized water. The sealed autoclave was then transferred into an oven kept at 160 ˚C and taken out after 4 h. After the autoclave was cooled to room temperature, the black product was separated by centrifugation at 6,000 rpm for 10 min. The precipitate was then washed once with $NH_3{\cdot}H_2O$ (9%) and five times with deionized water. The loading amounts of potassium halide, $NiCl_2$ and K_2PtCl_4 of other samples are listed in Table 1. Pt NCs were also synthesized with a similar method and the detailed procedure is included in the Methods section of the ESM.

4.3 HAc treatment and preparation of Pt–Ni alloy NCs/carbon black composites

The as-obtained black product was dispersed in HAc (99.9%) and treated with ultrasound for 5 h. The NCs were then collected by centrifugation at 6,000 rpm for 10 min and re-dispersed in ethanol. Carbon black with four times the weight of metal was then added to the ethanol dispersion and the mixture was treated with ultrasound for another 5 h. The NCs/carbon black composites were then collected by centrifugation. The loading ratio of total metal of the final composites was 20 wt.%. Finally, the composites were dispersed in 2 mL of ethanol for further electrochemical tests.

4.4 Hydrothermal syntheses of Pt-Co and Pt-Fe NCs

The hydrothermal method above was used to synthesize Pt–Co and Pt–Fe NCs by replacing $NiCl_2$ with equal amounts of $CoCl_2$ and $FeSO_4$. Table S3 (in the ESM) lists the feeding amounts of metallic precursors for every sample. HAc treatment was used for every sample after the hydrothermal synthesis.

4.5 Electrochemical analysis

The electrochemical tests were conducted on PGSTAT302N (Autolab Corp. Switzerland) electrochemical analyzer with impedance module, together with a glassy carbon RDE (5 mm in diameter) setup (Pine, U.S.) as the working electrode, a saturated Ag/AgCl reference electrode and a Pt foil as counter electrode. All of the potentials in this work are reported against RHE. 10 μL of an ethanol dispersion of the as-mentioned "acid treated" sample or commercial Pt/C (1 $mg_{Pt}{\cdot}mL^{-1}$) was dropped on the RDE and dried. UV–ozone treatment [33, 43] was then carried out by

illuminating the RDE with a UV lamp (10 W, with 185 and 254 nm emissions) at a distance of ~5 mm for 5 h. Then 5 μL of Nafion (0.2 wt.% ethanol solution) was dropped on RDE and dried, followed by rinsing the RDE with ultrapure water. 0.1 M $HClO_4$ was used as electrolyte. The CV tests were conducted in N_2 saturated electrolyte with a scan speed of 50 mV·s^{-1}. The ORR polarization curves were collected in O_2 saturated electrolyte in the anodic voltammetric scan with a speed of 20 mV·s^{-1}. The capacitance current was collected in N_2 saturated 0.1 M $HClO_4$ with the same scan speed in advance and was subtracted from the ORR polarization curve. Six ORR polarization curves were collected with the RDE rotation speed of 2,500, 1,600, 900 and 400 rpm for one sample, and the kinetic currents were calculated from Koutecky–Levich plots. 10,000 cycles of CV scans in the range of 0.6–1.0 V vs. RHE with a scan speed of 200 mV·s^{-1} in O_2 saturated electrolyte were carried out as the accelerated aging tests for each sample. CO stripping and H-UPD were used to measure the ECSA of the catalysts. For CO monolayer deposition, the potential of the working electrode was first kept at 0.1 V vs. RHE. The electrolyte was bubbled with CO for 5 min and then N_2 for 10 min. Then voltammetric sweeps from 0.05 to 1.25 V vs. RHE were collected with a scan speed of 50 mV·s^{-1}. To correct the iR-drop, impedance measurements at 0.68 V with the potential amplitude of 10 mV were applied with frequencies from 100 kHz to 1 Hz on a logarithmic scale, and the resistance of the system was deduced from the real component value of the impedance at the minimum of the Nyquist plot [68]. For each kind of catalyst, the electrochemical properties were obtained from three independent measurements.

4.6 Characterization

Samples for TEM characterization were prepared by drying a drop of sample dispersed in ethanol on an ultra-thin carbon film supported by a copper grid. TEM and HRTEM images were obtained on an FEI Tecnai F30 operated at 300 kV. HAADF-STEM images and EDS-mappings were obtained from an FEI TITAN Cs-corrected ChemiSTEM operated at 200 kV, which incorporated a probe corrector and a super-X EDS system. The average thicknesses of the Pt-enriched shells were calculated from six EDS line profiles collected on three alloy NCs for every sample. The XPS spectra were obtained from an Axis Ultra (Kratos, Japan) imaging photoelectron spectrometer. XRD patterns were collected on an X'Pert PRO diffractometer (Philips, Netherland) using Cu Kα radiation with a scan speed of 3°·min^{-1}. The contribution of the Kα_2 line was subtracted. ICP–AES analysis was conducted on a Profile Spec ICP–AES spectrometer (Leeman, U.S.).

Acknowledgements

We thank Prof. Dechun Zou and Mr. Ming Peng for their help with electrochemical characterization. This work was supported by the National Natural Science Foundation of China (Nos. 21025101, 21271011, and 21321001). Y. W. Z. particularly appreciates the financial aid from the China National Funds for Distinguished Young Scientists from the National Natural Science Foundation of China (NSFC). The work on microscopy was partly carried out in the Center of Electron Microscopy of Zhejiang University, which was financially supported by the National Natural Science Foundation of China (No. 51222202), the National Basic Research Program of China (No. 2014CB932500) and the Program for Innovative Research Teams in Universities of Ministry of Education of China (No. IRT13037) and the Fundamental Research Funds for the Central Universities (No. 2014XZZX003-07).

Electronic Supplementary Material: Supplementary material (more experimental details containing sample synthesis and characterization including XRD, TEM, STEM, EDS, TGA, FT-IR, XPS and electrochemical tests) is available in the online version of this article at http://dx.doi.org/10.1007/s12274-014-0632-7.

References

[1] Debe, M. K. Electrocatalyst approaches and challenges for automotive fuel cells. *Nature* **2012**, *486*, 43–51.

[2] Feng, J.; Liang, Y. Y.; Wang, H. L.; Li, Y. G.; Zhang, B.; Zhou, J. G.; Wang, J.; Regier, T.; Dai, H. J. Engineering manganese oxide/nanocarbon hybrid materials for oxygen reduction electrocatalysis. *Nano Res.* **2012**, *5*, 718–725.

[3] Liu, Z. Y.; Zhang, G. X.; Lu, Z. Y.; Jin, X. Y.; Chang, Z.; Sun, X. M. One-step scalable preparation of N-doped nanoporous carbon as a high-performance electrocatalyst for the

oxygen reduction reaction. *Nano Res.* **2013**, *6*, 293–301.

[4] Si, W. F.; Li, J.; Li, H. Q.; Li, S. S.; Yin, J.; Xu, H.; Guo, X. W.; Zhang, T.; Song, Y. J. Light-controlled synthesis of uniform platinum nanodendrites with markedly enhanced electrocatalytic activity. *Nano Res.* **2013**, *6*, 720–725.

[5] Rossmeisl, J.; Karlberg, G. S.; Jaramillo, T.; Norskov, J. K. Steady state oxygen reduction and cyclic voltammetry. *Faraday Discuss.* **2008**, *140*, 337–346.

[6] Greeley, J.; Stephens, I. E. L.; Bondarenko, A. S.; Johansson, T. P.; Hansen, H. A.; Jaramillo, T. F.; Rossmeisl, J.; Chorkendorff, I.; Nørskov, J. K. Alloys of platinum and early transition metals as oxygen reduction electrocatalysts. *Nat. Chem.* **2009**, *1*, 552–556.

[7] Koper, M. T. M. Thermodynamic theory of multi-electron transfer reactions: Implications for electrocatalysis. *J. Electroanal. Chem.* **2011**, *660*, 254–260.

[8] Wang, C.; Markovic, N. M.; Stamenkovic, V. R. Advanced platinum alloy electrocatalysts for the oxygen reduction reaction. *ACS Catal.* **2012**, *2*, 891–898.

[9] Stamenkovic, V. R.; Mun, B. S.; Arenz, M.; Mayrhofer, K. J. J.; Lucas, C. A.; Wang, G. F.; Ross, P. N.; Markovic, N. M. Trends in electrocatalysis on extended and nanoscale Pt-bimetallic alloy surfaces. *Nat. Mater.* **2007**, *6*, 241–247.

[10] Stamenkovic, V. R.; Fowler, B.; Mun, B. S.; Wang, G. F.; Ross, P. N.; Lucas, C. A.; Marković, N. M. Improved oxygen reduction activity on $Pt_3Ni(111)$ via increased surface site availability. *Science* **2007**, *315*, 493–497.

[11] Stamenkovic, V.; Mun, B. S.; Mayrhofer, K. J. J.; Ross, P. N.; Markovic, N. M.; Rossmeisl, J.; Greeley, J.; Nørskov, J. K. Changing the activity of electrocatalysts for oxygen reduction by tuning the surface electronic structure. *Angew. Chem. Int. Ed.* **2006**, *45*, 2897–2901.

[12] van der Vliet, D. F.; Wang, C.; Tripkovic, D.; Strmcnik, D.; Zhang, X. F.; Debe, M. K.; Atanasoski, R. T.; Markovic, N. M.; Stamenkovic, V. R. Mesostructured thin films as electrocatalysts with tunable composition and surface morphology. *Nat. Mater.* **2012**, *11*, 1051–1058.

[13] Zhang, C. L.; Hwang, S. Y.; Trout, A.; Peng, Z. M. Solid-state chemistry-enabled scalable production of octahedral Pt–Ni alloy electrocatalyst for oxygen reduction reaction. *J. Am. Chem. Soc.* **2014**, *136*, 7805–7808.

[14] Xin, H. L.; Holewinski, A.; Schweitzer, N.; Nikolla, E.; Linic, S. Electronic structure engineering in heterogeneous catalysis: Identifying novel alloy catalysts based on rapid screening for materials with desired electronic properties. *Top. Catal.* **2012**, *55*, 376–390.

[15] Strasser, P.; Koh, S.; Anniyev, T.; Greeley, J.; More, K.; Yu, C. F.; Liu, Z. C.; Kaya, S.; Nordlund, D.; Ogasawara, H.; Toney, M. F.; Nilsson, A. Lattice-strain control of the activity in dealloyed core-shell fuel cell catalysts. *Nat. Chem.* **2010**, *2*, 454–460.

[16] Kuttiyiel, K. A.; Sasaki, K.; Choi, Y.; Su, D.; Liu, P.; Adzic, R. R. Nitride stabilized PtNi core–shell nanocatalyst for high oxygen reduction activity. *Nano Lett.* **2012**, *12*, 6266–6271.

[17] Sun, S. H.; Murray, C. B.; Weller, D.; Folks, L.; Moser, A. Monodisperse FePt nanoparticles and ferromagnetic FePt nanocrystal superlattices. *Science* **2000**, *287*, 1989–1992.

[18] Wang, C.; Hou, Y. L.; Kim, J.; Sun, S. H. A general strategy for synthesizing FePt nanowires and nanorods. *Angew. Chem. Int. Ed.* **2007**, *46*, 6333–6335.

[19] Shevchenko, E. V.; Talapin, D. V.; Rogach, A. L.; Kornowski, A.; Haase, M.; Weller, H. Colloidal synthesis and self-assembly of $CoPt_3$ nanocrystals. *J. Am. Chem. Soc.* **2002**, *124*, 11480–11485.

[20] Ahrenstorf, K.; Albrecht, O.; Heller, H.; Kornowski, A.; Görlitz, D.; Weller, H. Colloidal synthesis of Ni_xPt_{1-x} nanoparticles with tuneable composition and size. *Small* **2007**, *3*, 271–274.

[21] Wang, C.; van der Vliet, D.; Chang, K. C.; You, H.; Strmcnik, D.; Schlueter, J. A.; Markovic, N. M.; Stamenkovic, V. R. Monodisperse Pt_3Co nanoparticles as a catalyst for the oxygen reduction reaction: Size-dependent activity. *J. Phys. Chem. C* **2009**, *113*, 19365–19368.

[22] Wu, J. B.; Yang, H. Synthesis and electrocatalytic oxygen reduction properties of truncated octahedral Pt_3Ni nanoparticles. *Nano Res.* **2011**, *4*, 72–82.

[23] Zhang, J.; Fang, J. Y. A general strategy for preparation of Pt 3d-transition metal (Co, Fe, Ni) nanocubes. *J. Am. Chem. Soc.* **2009**, *131*, 18543–18547.

[24] Zhang, J.; Yang, H. Z.; Fang, J. Y.; Zou, S. Z. Synthesis and oxygen reduction activity of shape-controlled Pt_3Ni nanopolyhedra. *Nano Lett.* **2010**, *10*, 638–644.

[25] Wu, J. B.; Gross, A.; Yang, H. Shape and composition-controlled platinum alloy nanocrystals using carbon monoxide as reducing agent. *Nano Lett.* **2011**, *11*, 798–802.

[26] Wu, J. B.; Qi, L.; You, H. J.; Gross, A.; Li, J.; Yang, H. Icosahedral platinum alloy nanocrystals with enhanced electrocatalytic activities. *J. Am. Chem. Soc.* **2012**, *134*, 11880–11883.

[27] Li, D. G.; Wang, C.; Tripkovic, D.; Sun, S. H.; Markovic, N. M.; Stamenkovic, V. R. Surfactant removal for colloidal nanoparticles from solution synthesis: The effect on catalytic performance. *ACS Catal.* **2012**, *2*, 1358–1362.

[28] Wang, C.; Wang, G. F.; van der Vliet, D.; Chang, K. C.; Markovic, N. M.; Stamenkovic, V. R. Monodisperse Pt_3Co nanoparticles as electrocatalyst: The effects of particle size and pretreatment on electrocatalytic reduction of oxygen.

Phys. Chem. Chem. Phys. **2010**, *12*, 6933–6939.

[29] Wang, C.; Chi, M. F.; Li, D. G.; Strmcnik, D.; van der Vliet, D.; Wang, G. F.; Komanicky, V.; Chang, K. C.; Paulikas, A. P.; Tripkovic, D. et al. Design and synthesis of bimetallic electrocatalyst with multilayered Pt-skin surfaces. *J. Am. Chem. Soc.* **2011**, *133*, 14396–14403.

[30] Durst, J.; Lopez-Haro, M.; Dubau, L.; Chatenet, M.; Soldo-Olivier, Y.; Guétaz, L.; Bayle-Guillemaud, P.; Maillard, F. Reversibility of Pt-skin and Pt-skeleton nanostructures in acidic media. *J. Phys. Chem. Lett.* **2014**, *5*, 434–439.

[31] Chen, C.; Kang, Y. J.; Huo, Z. Y.; Zhu, Z. W.; Huang, W. Y.; Xin, H. L. L.; Snyder, J. D.; Li, D. G.; Herron, J. A.; Mavrikakis, M. et al. Highly crystalline multimetallic nanoframes with three-dimensional electrocatalytic surfaces. *Science* **2014**, *343*, 1339–1343.

[32] Wu, Y. E.; Cai, S. F.; Wang, D. S.; He, W.; Li, Y. D. Syntheses of water-soluble octahedral, truncated octahedral, and cubic Pt–Ni nanocrystals and their structure–activity study in model hydrogenation reactions. *J. Am. Chem. Soc.* **2012**, *134*, 8975–8981.

[33] Wu, Y. E.; Wang, D. S.; Niu, Z. Q.; Chen, P. C.; Zhou, G.; Li, Y. D. A strategy for designing a concave Pt–Ni alloy through controllable chemical etching. *Angew. Chem. Int. Ed.* **2012**, *51*, 12524–12528.

[34] Wu, Y. E.; Wang, D. S.; Chen, X. B.; Zhou, G.; Yu, R.; Li, Y. D. Defect-dominated shape recovery of nanocrystals: A new strategy for trimetallic catalysts. *J. Am. Chem. Soc.* **2013**, *135*, 12220–12223.

[35] Carpenter, M. K.; Moylan, T. E.; Kukreja, R. S.; Atwan, M. H.; Tessema, M. M. Solvothermal synthesis of platinum alloy nanoparticles for oxygen reduction electrocatalysis. *J. Am. Chem. Soc.* **2012**, *134*, 8535–8542.

[36] Cui, C. H.; Gan, L.; Li, H. H.; Yu, S. H.; Heggen, M.; Strasser, P. Octahedral PtNi nanoparticle catalysts: Exceptional oxygen reduction activity by tuning the alloy particle surface composition. *Nano Lett.* **2012**, *12*, 5885–5889.

[37] Zhu, H. Y.; Zhang, S.; Guo, S. J.; Su, D.; Sun, S. H. Synthetic control of FePt*M* nanorods (*M* = Cu, Ni) to enhance the oxygen reduction reaction. *J. Am. Chem. Soc.* **2013**, *135*, 7130–7133.

[38] Stevens, D. A.; Mehrotra, R.; Sanderson, R. J.; Vernstrom, G. D.; Atanasoski, R. T.; Debe, M. K.; Dahn, J. R. Dissolution of Ni from high Ni content $Pt_{1-x}Ni_x$ alloys. *J. Electrochem. Soc.* **2011**, *158*, B905–B909.

[39] Wang, C.; Chi, M. F.; Wang, G. F.; van der Vliet, D.; Li, D. G.; More, K.; Wang, H. H.; Schlueter, J. A.; Markovic, N. M.; Stamenkovic, V. R. Correlation between surface chemistry and electrocatalytic properties of monodisperse Pt_xNi_{1-x} nanoparticles. *Adv. Funct. Mater.* **2011**, *21*, 147–152.

[40] Gan, L.; Heggen, M.; Rudi, S.; Strasser, P. Core–shell compositional fine structures of dealloyed Pt_xNi_{1-x} nanoparticles and their impact on oxygen reduction catalysis. *Nano Lett.* **2012**, *12*, 5423–5430.

[41] Oezaslan, M.; Heggen, M.; Strasser, P. Size-dependent morphology of dealloyed bimetallic catalysts: Linking the nano to the macro scale. *J. Am. Chem. Soc.* **2012**, *134*, 514–524.

[42] Gan, L.; Heggen, M.; O'Malley, R.; Theobald, B.; Strasser, P. Understanding and controlling nanoporosity formation for improving the stability of bimetallic fuel cell catalysts. *Nano Lett.* **2013**, *13*, 1131–1138.

[43] Cui, C. H.; Gan, L.; Heggen, M.; Rudi, S.; Strasser, P. Compositional segregation in shaped Pt alloy nanoparticles and their structural behaviour during electrocatalysis. *Nat. Mater.* **2013**, *12*, 765–771.

[44] Wang, C.; van der Vliet, D.; More, K. L.; Zaluzec, N. J.; Peng, S.; Sun, S. H.; Daimon, H.; Wang, G. F.; Greeley, J.; Pearson, J. et al. Multimetallic Au/$FePt_3$ nanoparticles as highly durable electrocatalyst. *Nano Lett.* **2011**, *11*, 919–926.

[45] Guo, S. J.; Zhang, S.; Su, D.; Sun, S. H. Seed-mediated synthesis of core/shell FePt*M*/FePt (*M* = Pd, Au) nanowires and their electrocatalysis for Oxygen Reduction Reaction. *J. Am. Chem. Soc.* **2013**, *135*, 13879–13884.

[46] Johnson, R. A. Alloy models with the embedded-atom method. *Phys. Rev. B* **1989**, *39*, 12554–12559.

[47] Wang, Z. L. Transmission electron microscopy of shape-controlled nanocrystals and their assemblies. *J. Phys. Chem. B* **2000**, *104*, 1153–1175.

[48] Xia, Y. N.; Xiong, Y. J.; Lim, B.; Skrabalak, S. E. Shape-controlled synthesis of metal nanocrystals: Simple chemistry meets complex physics? *Angew. Chem. Int. Ed.* **2009**, *48*, 60–103.

[49] Yin, A. X.; Min, X. Q.; Zhang, Y. W.; Yan, C. H. Shape-selective synthesis and facet-dependent enhanced electrocatalytic activity and durability of monodisperse sub-10 nm Pt−Pd tetrahedrons and cubes. *J. Am. Chem. Soc.* **2011**, *133*, 3816–3819.

[50] Huang, X. Q.; Li, Y. J.; Li, Y. J.; Zhou, H. L.; Duan, X. F.; Huang, Y. Synthesis of PtPd bimetal nanocrystals with controllable shape, composition, and their tunable catalytic properties. *Nano Lett.* **2012**, *12*, 4265–4270.

[51] Yin, A. X.; Min, X. Q.; Zhu, W.; Liu, W. C.; Zhang, Y. W.; Yan, C. H. Pt–Cu and Pt–Pd–Cu concave nanocubes with high-index facets and superior electrocatalytic activity. *Chem. Eur. J.* **2012**, *18*, 777–782.

[52] Zhang, H.; Jin, M. S.; Wang, J. G.; Li, W. Y.; Camargo, P. H. C.; Kim, M. J.; Yang, D. R.; Xie, Z. X.; Xia, Y. A. Synthesis of Pd−Pt bimetallic nanocrystals with a concave structure

through a bromide-induced galvanic replacement reaction. *J. Am. Chem. Soc.* **2011**, *133*, 6078–6089.

[53] Toda, T.; Igarashi, H.; Uchida, H.; Watanabe, M. Enhancement of the electroreduction of oxygen on Pt alloys with Fe, Ni, and Co. *J. Electrochem. Soc.* **1999**, *146*, 3750–3756.

[54] Ahmadi, M.; Behafarid, F.; Cui, C. H.; Strasser, P.; Cuenya, B. R. Long-range segregation phenomena in shape-selected bimetallic nanoparticles: Chemical state effects. *ACS Nano* **2013**, *7*, 9195–9204.

[55] Grosvenor, A. P.; Biesinger, M. C.; Smart, R. S.; McIntyre, N. S. New interpretations of XPS spectra of nickel metal and oxides. *Surf. Sci.* **2006**, *600*, 1771–1779.

[56] Bera, P.; Priolkar, K. R.; Gayen, A.; Sarode, P. R.; Hegde, M. S.; Emura, S.; Kumashiro, R.; Jayaram, V.; Subbanna, G. N. Ionic dispersion of Pt over CeO_2 by the combustion method: Structural investigation by XRD, TEM, XPS, and EXAFS. *Chem. Mater.* **2003**, *15*, 2049–2060.

[57] Porsgaard, S.; Merte, L. R.; Ono, L. K.; Behafarid, F.; Matos, J.; Helveg, S.; Salmeron, M.; Cuenya, B. R.; Besenbacher, F. Stability of platinum nanoparticles supported on SiO_2/Si(111): A high-pressure X-ray photoelectron spectroscopy study. *ACS Nano* **2012**, *6*, 10743–10749.

[58] Chen, W.; Kim, J.; Sun, S. H.; Chen, S. W. Electro-oxidation of formic acid catalyzed by FePt nanoparticles. *Phys. Chem. Chem. Phys.* **2006**, *8*, 2779–2786.

[59] Yin, A. X.; Min, X. Q.; Zhu, W.; Wu, H. S.; Zhang, Y. W.; Yan, C. H. Multiply twinned Pt-Pd nanoicosahedrons as highly active electrocatalysts for methanol oxidation. *Chem. Commun.* **2012**, *48*, 543–545.

[60] van der Vliet, D. F.; Wang, C.; Li, D. G.; Paulikas, A. P.; Greeley, J.; Rankin, R. B.; Strmcnik, D.; Tripkovic, D.; Markovic, N. M.; Stamenkovic, V. R. Unique electrochemical adsorption properties of Pt-skin surfaces. *Angew. Chem. Int. Ed.* **2012**, *51*, 3139–3142.

[61] Choi, S. I.; Xie, S. F.; Shao, M. H.; Odell, J. H.; Lu, N.; Peng, H. C.; Protsailo, L.; Guerrero, S.; Park, J. H.; Xia, X. H. et al. Synthesis and characterization of 9 nm Pt–Ni octahedra with a record high activity of 3.3 A/mg(Pt) for the oxygen reduction reaction. *Nano Lett.* **2013**, *13*, 3420–3425.

[62] Mazumder, V.; Chi, M. F.; More, K. L.; Sun, S. H. Core/shell Pd/FePt nanoparticles as an active and durable catalyst for the oxygen reduction reaction. *J. Am. Chem. Soc.* **2010**, *132*, 7848–7849.

[63] Sun, X. L.; Li, D. G.; Ding, Y.; Zhu, W. L.; Guo, S. J.; Wang, Z. L.; Sun, S. H. Core/shell Au/CuPt nanoparticles and their dual electrocatalysis for both reduction and oxidation reactions. *J. Am. Chem. Soc.* **2014**, *136*, 5745–5749.

[64] Zhang, S.; Zhang, X.; Jiang, G. M.; Zhu, H. Y.; Guo, S. J.; Su, D.; Lu, G.; Sun, S. H. Tuning nanoparticle structure and surface strain for catalysis optimization. *J. Am. Chem. Soc.* **2014**, *136*, 7734–7739.

[65] Zhang, J.; Sasaki, K.; Sutter, E.; Adzic, R. R. Stabilization of platinum oxygen-reduction electrocatalysts using gold clusters. *Science* **2007**, *315*, 220–222.

[66] Fu, G. T.; Liu, Z. Y.; Chen, Y.; Lin, J.; Tang, Y. W.; Lu, T. H. Synthesis and electrocatalytic activity of Au@Pd core-shell nanothorns for the Oxygen Reduction Reaction. *Nano Res.* **2014**, *7*, 1205–1214.

[67] Zheng, F. L.; Wong, W. T.; Yung, K. F. Facile design of Au@Pt core-shell nanostructures: Formation of Pt sub-monolayers with tunable coverage and their applications in electrocatalysis. *Nano Res.* **2014**, *7*, 410–417.

[68] van der Vliet, D.; Strmcnik, D. S.; Wang, C.; Stamenkovic, V. R.; Markovic, N. M.; Koper, M. T. M. On the importance of correcting for the uncompensated Ohmic resistance in model experiments of the oxygen reduction reaction. *J. Electroanal. Chem.* **2010**, *647*, 29–34.